

1
2 **Title: Monitoring land surface albedo and vegetation dynamics using high spatial**
3 **and temporal resolution synthetic time series from Landsat and the MODIS**
4 **BRDF/NBAR/albedo product**

5
6
7 **Authors:** Zhuosen Wang^{1,3*}, Crystal B. Schaaf², Qingsong Sun², JiHyun Kim⁴, Angela M. Erb²,
8 Feng Gao⁵, Miguel O. Román³, Yun Yang⁵, Shelley Petroy⁶, Jeffrey R. Taylor⁷, Jeffrey G.
9 Masek³, Jeffrey T. Morisette⁸, Xiaoyang Zhang⁹, Shirley A. Papuga¹⁰

10
11 **Affiliations:**

12
13 ¹Earth System Science Interdisciplinary Center, University of Maryland College Park, College Park, MD, USA

14
15 ²School for the Environment, University of Massachusetts Boston, Boston, MA, USA.

16
17 ³NASA Goddard Space Flight Center, Greenbelt, MD, USA.

18
19 ⁴Department of Geography, Indiana University Bloomington, Bloomington, IN, USA.

20
21 ⁵ USDA, Agricultural Research Service, Hydrology and Remote Sensing Laboratory, Beltsville, MD, USA

22
23 ⁶National Ecological Observatory Network, Boulder, CO, USA.

24
25 ⁷Institute of Technology Campus, Nova Scotia Community College, Halifax, NS, Canada

26
27 ⁸U.S. Geological Survey, Department of the Interior North Central Climate Science Center, Fort Collins, CO, USA

28
29 ⁹Geospatial Sciences Center of Excellence, South Dakota State University, Brookings, SD, USA.

30
31 ¹⁰School of Natural Resources and the Environment, University of Arizona, Tucson, Arizona, USA.

32
33 *Correspondence to: zhuosen.wang@nasa.gov

34
35
36 **Key words:** Albedo; Vegetation Index; Data Fusion; Phenology; Remote sensing

37
38
39 **Key points:**

- 40
41 1. Synthetic time series of albedo and EVI can capture land surface dynamics with high
42 similarity to tower and field data.
43 2. The RMSE and bias of the synthetic albedo values are less than 0.013 and within ± 0.006 ,
44 respectively as compared to Ameiflux field data
45 3. In the future access to spatially representative NEON tower albedometer data will greatly
46 improve our ability to evaluate moderate resolution satellite products.

50 **Abstract:**

51

52 Seasonal vegetation phenology can significantly alter surface albedo which in turn affects the
53 global energy balance and the albedo warming/cooling feedbacks that impact climate change. To
54 monitor and quantify the surface dynamics of heterogeneous landscapes, high temporal and
55 spatial resolution synthetic time series of albedo and the enhanced vegetation index (EVI) were
56 generated from the 500 m Moderate Resolution Imaging Spectroradiometer (MODIS)
57 operational Collection V006 daily BRDF/NBAR/albedo products and 30 m Landsat 5 albedo and
58 near-nadir reflectance data through the use of the Spatial and Temporal Adaptive Reflectance
59 Fusion Model (STARFM). The traditional Landsat Albedo (Shuai et al., 2011) makes use of the
60 MODIS BRDF/Albedo products (MCD43) by assigning appropriate BRDFs from coincident
61 MODIS products to each Landsat image to generate a 30 m Landsat albedo product for that
62 acquisition date. The available cloud free Landsat 5 albedos (due to clouds, generated every 16
63 days at best) were used in conjunction with the daily MODIS albedos to determine the
64 appropriate 30 m albedos for the intervening daily time steps in this study. These enhanced daily
65 30 m spatial resolution synthetic time series were then used to track albedo and vegetation
66 phenology dynamics over three Ameriflux tower sites (Harvard Forest in 2007, Santa Rita in
67 2011 and Walker Branch in 2005). These Ameriflux sites were chosen as they are all quite
68 nearby new towers coming on line for the National Ecological Observatory Network (NEON),
69 and thus represent locations which will be served by spatially paired albedo measures in the near
70 future. The availability of data from the NEON towers will greatly expand the sources of tower
71 albedometer data available for evaluation of satellite products. At these three Ameriflux tower
72 sites the synthetic time series of broadband shortwave albedos were evaluated using the tower
73 albedo measurements with a Root Mean Square Error (RMSE) less than 0.013 and a bias within
74 the range of ± 0.006 . These synthetic time series provide much greater spatial detail than the 500
75 m gridded MODIS data, especially over more heterogeneous surfaces, which improves the
76 efforts to characterize and monitor the spatial variation across species and communities. The
77 mean of the difference between maximum and minimum synthetic time series of albedo within
78 the MODIS pixels over a subset of satellite data of Harvard Forest (16 km by 14 km) was as high
79 as 0.2 during the snow-covered period and reduced to around 0.1 during the snow-free period.
80 Similarly, we have used STARFM to also couple MODIS Nadir BRDF Adjusted Reflectances

81 (NBAR) values with Landsat 5 reflectances to generate daily synthetic times series of NBAR and
82 thus Enhanced Vegetation Index (NBAR-EVI) at a 30 m resolution. While normally STARFM is
83 used with directional reflectances, the use of the view angle corrected daily MODIS NBAR
84 values will provide more consistent time series. These synthetic times series of EVI are shown to
85 capture seasonal vegetation dynamics with finer spatial and temporal details, especially over
86 heterogeneous land surfaces.

87

88 **1. Introduction**

89

90 Global surface temperatures have increased by approximately 0.6°C in the past three decades
91 (Hansen et al., 2010, 2006). This warming has contributed to a lengthening of the terrestrial
92 vegetation growing season, especially in the mid- and high latitudes (Körner and Basler, 2010;
93 Menzel and Fabian, 1999; Menzel et al., 2006; Myneni et al., 1997). Changes in the timing of
94 leaf-out impact essential ecosystem processes; therefore accurate monitoring of phenology is
95 required to understand the variability in terrestrial ecosystem change (Baldocchi et al., 2001;
96 Churkina et al., 2005; Cleland et al., 2006; Piao et al., 2007; Richardson et al., 2012, 2009).

97

98 Land surface albedo plays a crucial role in land surface climate and biosphere models as a key
99 climate forcing variable (Dirmeyer and Shukla, 1994; Hall, 2004; Lofgren, 1995; Ollinger et al.,
100 2008). Typical surface albedo can range from as high as 0.8 over a pure snow-covered area to as
101 low as 0.1 over vegetation during the snow-free period (Jin et al., 2002). This suggests that
102 climate-driven changes in phenology (e.g. the onset of spring and snowmelt) may result in
103 significant changes in the surface albedo. At lower albedo, the surface absorbs more solar energy
104 and increases the local surface temperature which in turn affects the timing of phenological
105 events (Richardson et al., 2013). This surface albedo feedback loop perpetuates further warming
106 and climate change.

107

108 Trend analysis of vegetation albedo and phenology has been previously carried out using the
109 high temporal resolution 500 m gridded MODIS albedo and Nadir Bidirectional Reflectance
110 Distribution Function (BRDF)-Adjusted Reflectance (NBAR)-derived Vegetation Indices (VI)
111 (Friedl et al., 2014; Ganguly et al., 2010; Zhang et al., 2003)]. The MODIS 500 m

112 BRDF/NBAR/albedo product (MCD43A) (Schaaf, 2008; Schaaf et al., 2011, 2002) provides
113 high quality surface reflectance anisotropy retrievals over a variety of land surface types with
114 high accuracy (Jin et al., 2003; Liang et al., 2002; Liu et al., 2009; Román et al., 2010, 2009;
115 Wang et al., 2012, 2014). MODIS NBAR (MCD43A4) standardizes the MODIS directional
116 reflectances to a nadir view at the illumination of local solar noon to eliminate the angular effect
117 on the biophysical related parameters.

118

119 However, there are limitations to the application of daily 500 m gridded MODIS products such
120 as NBAR and albedo in highly heterogeneous landscapes. Snow cover over different land types
121 within a single MODIS pixel may melt at different rates and the vegetation green-up within a
122 coarse satellite pixel of a mixed land cover type is usually dominated by the proportion of
123 vegetation with the earlier green-up times (Zhang et al., 2017). As such, enhanced high
124 resolution temporal and spatial data are critical to enable more detailed phenological monitoring
125 (Liang et al., 2014). A persistent issue with current remotely sensed data is that sensors capture
126 either high spatial resolution and low temporal resolution (e.g. Landsat, ASTER) or coarser
127 spatial resolution and higher temporal resolution (e.g. MODIS, VIIRS). This limits the ability to
128 monitor rapid land surface processes, particularly in heterogeneous landscapes. Several
129 algorithms have been developed to blend these two resolutions of datasets to generate high
130 temporal and spatial resolution surface reflectance (Emelyanova et al., 2013; Gao et al., 2006;
131 Hilker et al., 2009; Roy et al., 2008; Zhu et al., 2010; Zurita-Milla et al., 2009). The Spatial and
132 Temporal Adaptive Reflectance Fusion Model (STARFM) (Gao et al., 2006) has been
133 successfully applied to generate high spatial and temporal resolution reflectance time series by
134 combining cloud-free Landsat and MODIS reflectance data for vegetation monitoring. In this
135 study, the STARFM algorithm is utilized to produce high spatial and temporal resolution albedo
136 and VI time series by fusing Landsat and MODIS data.

137

138 Essential in the development of accurate satellite-driven remotely sensed products is the need for
139 ground validation over various land covers, temporal scales, and seasonal dynamics over the
140 long-term. In order to examine the ability of long-term field and tower networks such as
141 Ameriflux and specifically the new National Ecological Observation Network (NEON) to
142 provide *in situ* reference data for MODIS and other moderate resolution satellite sensors, we

143 present here an analysis of the spatial representativeness of the 20 core NEON terrestrial tower
144 sites and thus their suitability to serve as moderate resolution albedo evaluation sites. NEON is a
145 comprehensive observatory network designed to monitor physical and chemical properties of
146 climate-related processes, including airborne remote sensing measurements, over the U.S.
147 continental-scale ecosystem (Kampe, 2010; Keller et al., 2008). NEON sites are designed and
148 sited to obtain accurate flux measurements, but the tower locations for other tower-based
149 measurements such as albedo are not necessarily well suited for the evaluation of coarse
150 resolution satellite acquisitions. Thus the STARFM method is used to generate synthetic high
151 resolution albedo as well as NBAR-based vegetation indices at several select Ameriflux sites that
152 are in close proximity to core NEON sites. This is done both to further demonstrate the
153 enhancement that coupled MODIS-Landsat data products (including albedo and NBAR) provide
154 for the detection of land surface characteristics and to illustrate the value of the increasingly
155 available NEON tower data for satellite product validation over a wide range of ecosystems.

156

157 Thus the objectives of this study are to investigate the representativeness of tower measurements
158 from NEON for the validation of moderate spatial resolution albedo products (e.g. MODIS,
159 VIIRS) and demonstrate the concept of improving the ability to monitor temporal vegetation
160 variations at the landscape scale especially heterogeneous surface by using STARFM to generate
161 high temporal (daily) and spatial (30m) resolution albedo and NBAR-derived vegetation indices
162 from the Collection V006 MODIS BRDF/NBAR/albedo products and Landsat 5 data.

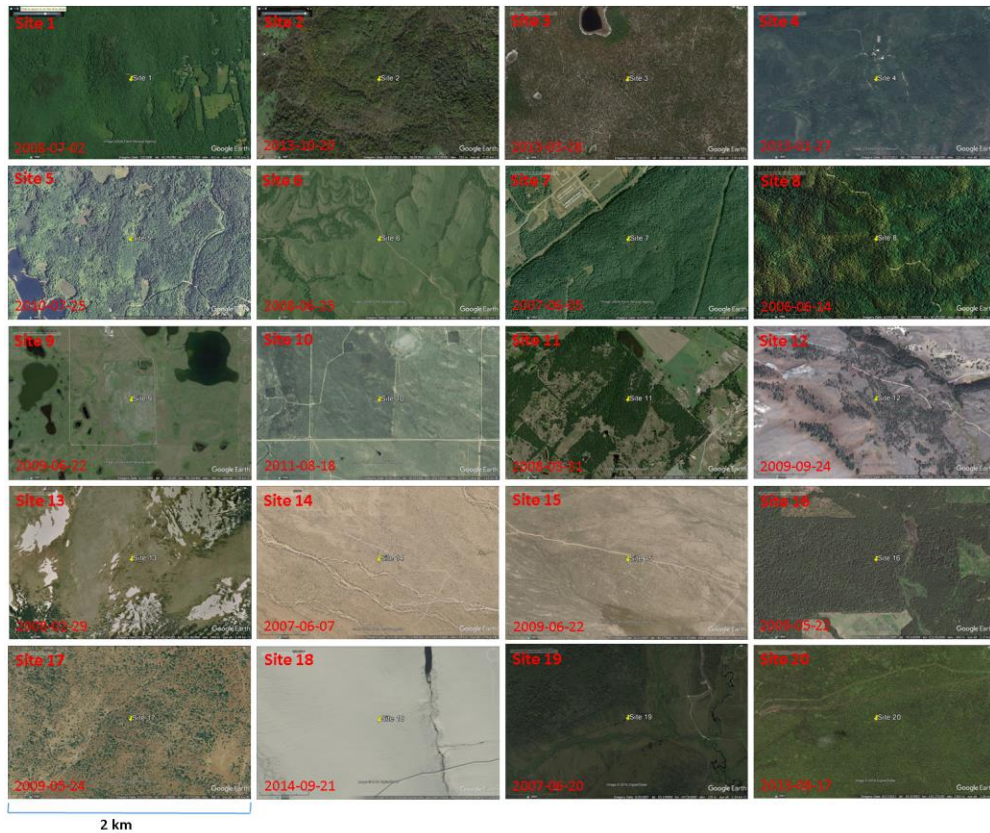
163

164 **2. Material and methodology**

165 **2.1 Study area and ground measurements**

166 NEON consists of 47 terrestrial tower sites located across 20 eco-climatic domains in the US
167 with one “core site” at each domain. Each of the 20 core terrestrial sites (Fig. 1) represents a
168 different ecosystem region with varying vegetation types and climates (Hamilton et al., 2007;
169 Kampe, 2010; Schimel et al., 2007). Long-term (30 year) data acquisition from NEON will
170 provide site-based field ecological and climatic observations which can be coupled with regional
171 and national-scale airborne remote sensing observations to describe land use and climate-driven
172 seasonal change. The NEON network is currently under construction (with only nine sites
173 starting to be operational), therefore we selected three Ameriflux tower sites (Harvard Forest,

174 Santa Rita and Walker Branch) (Table 1) which are located very close to NEON sites. These
175 Ameriflux sites have the same land cover type as their NEON counterparts and the distances
176 between the NEON and Ameriflux tower pairs are less than 0.8 km in all cases. The AmeriFlux
177 network, established by the Department of Energy (DOE), provides ecosystem level exchanges
178 of CO₂, water, and energy (including surface albedo) (Law et al., 2002; Running et al., 1999). In
179 this study the Ameriflux tower measurements were used to evaluate the daily high spatial
180 resolution synthetic time series of albedo. The Harvard Forest site is a mixed deciduous
181 broadleaf and evergreen needleleaf forest dominated by red maple (*Acer rubrum*), red oak
182 (*Quercus rubra*), birch (*Betula*), and hemlock (*Tsuga canadensis*). The Walker Branch site is
183 near the NEON Oak Ridge site and is a 50-year-old broadleaf forest stand dominated by oak
184 (*Quercus alba* L., *Q. prinus* L.), hickory (*Carya ovata*(Mill.) K. Koch), maple (*Acer rubrum* L.,
185 *A. saccharum*), and tulip poplar (*Liriodendron tulipifera* L.). Both of these Ameriflux towers are
186 mounted with Kipp and Zonen albedometers and radiometers to measure shortwave albedo. The
187 Santa Rita Creosote site is located near the NEON Santa Rita Experimental Range site. This
188 open shrub site is dominated by creosote bush (*Larrea tridentata*) and the shortwave albedo is
189 derived from a Kipp and Zonen four component radiometer (Sanchez-Mejia and Papuga, 2014;
190 Sanchez-Mejia et al., 2014). The local noon ground albedo is calculated as the ratio of upwelling
191 radiation and downwelling radiation. In addition, field measurements of green-up dates with full
192 bud break were obtained at the Harvard Forest site through the long-term ecological research
193 (LTER) network database (<http://www.lternet.edu/sites/hfr>) (Richardson and O'Keefe, 2009;
194 Zhang et al., 2006). Phenocam photos acquired at Santa Rita Creosote site were used to track the
195 vegetation dynamics.



196

197 Fig. 1 Landscapes and acquired dates of the 20 NEON core sites (from Google Earth).

198

199 Table 1: Characteristics of the three Ameriflux and 20 NEON tower sites in 20 NEON domains

Domain Number	Site Name	Network	Latitude/Longitude	State	Land type	Tower height (m)
D01	Harvard Forest	NEON	42.5369/-72.1727	Massachusetts	Mixed Forest	36
D01	Harvard Forest	Ameriflux	42.54378/-72.1715	Massachusetts	Mixed Forest	30
D02	Smithsonian Conservation Biology Institute	NEON	38.8929/-78.1395	Virginia	Deciduous broadleaf forest	50
D03	Ordway-Swisher Biological Station	NEON	29.6893/-81.9934	Florida	Evergreen broadleaf forest	33
D04	Guanica Forest	NEON	17.9696/-66.8687	Puerto Rico	Evergreen broadleaf forest	20
D05	University of Notre Dame Environmental	NEON	46.2339/-89.5373	Michigan	Mixed forest	36

	Research Center					
D06	Konza Prairie Biological Station	NEON	39.1008/-96.5631	Kansas	Prairie	8
D07	Oak Ridge	NEON	35.9641/-84.2826	Tennessee	Deciduous broadleaf forest	38
D07	Walker Branch	Ameriflux	35.9588/-84.2874	Tennessee	Deciduous broadleaf forest	44
D08	Talladega National Forest	NEON	32.9505/-87.3933	Alabama	Mixed forest	35
D09	Woodworth	NEON	47.1282/-99.2414	North Dakota	Grass	8
D10	Central Plains Experimental Range	NEON	40.8155/-104.7456	Colorado	grass	8
D11	LBJ National Grassland	NEON	33.4012/-97.5700	Texas	Deciduous broadleaf forest	22
D12	Yellowstone Northern Range (Frog Rock)	NEON	44.9535/-110.5391	Wyoming	Evergreen needleleaf forest	20
D13	Niwot Ridge Mountain Research Station	NEON	40.0543/-105.5824	Colorado	grass	8
D14	Santa Rita Experimental Range	NEON	31.9107/-110.8355	Arizona	shrub	8
D14	Santa Rita Creosote	Ameriflux	31.9083/-110.8396	Arizona	shrub	2.75
D15	Onaqui-Ault	NEON	40.1776/-112.4524	Utah	sagebrush steppe	8
D16	Wind River Experimental Forest	NEON	45.8205/-121.9519	Washington	Evergreen needleleaf forest	86
D17	San Joaquin Experimental Range	NEON	37.1088/-119.7323	California	open woodland	36
D18	Toolik Lake	NEON	68.6611/-149.3705	Alaska	tundra	8
D19	Caribou Creek - Poker Flats Watershed	NEON	65.1540/-147.5026	Alaska	Evergreen needleleaf forest	18
D20	Upper Waiakea Forest Reserve	NEON	19.5577/-155.2711	Hawaii	Evergreen broadleaf forest	20

200

201

2.2 Satellite Data

202 The 500 m Collection V006 MODIS BRDF/NBAR/albedo product (MCD43) and the 30 m
203 Landsat 5 surface reflectance were used for this synthetic study. The MODIS
204 BRDF/NBAR/albedo product makes use of a linear “kernel-driven” RossThick-LiSparse
205 Reciprocal (RTLSR) BRDF model which has been shown to be well suited to describe the
206 reflectance anisotropy of each pixel at a 500-m gridded resolution over a variety of land covers
207 (Lucht et al., 2000; Privette et al., 1997; Schaaf et al., 2002). In the past this multi-day product
208 was retrieved every 8 days which limited its ability to capture rapidly changing land surface
209 events such as vegetation emergence and snowmelt. However, the Collection V006 MODIS
210 BRDF/albedo product, currently in production, is now retrieved daily and represents the best
211 possible BRDF based on 16 days of input information. The day of interest is heavily weighted
212 within the algorithm to allow daily monitoring of land surface change phenomena (Schaaf et al.,
213 2011; Shuai et al., 2013; Wang et al., 2012).

214

215 The 30 m spatial resolution Landsat 5 surface reflectance over the three sites is derived from
216 Landsat Ecosystem Disturbance Adaptive Processing System (LEDAPS) (Masek et al., 2006).
217 The Landsat narrowband to broadband coefficients were applied to generate the shortwave
218 broadband surface reflectance (He et al., 2014; Shuai et al., 2014). Landsat shortwave albedo is
219 calculated from the Anisotropic Reflectance Factor (ARF) taken from a high quality MODIS
220 pixel associated with the same spectral cluster (Shuai et al., 2011; Wang et al., 2012). The Shuai
221 et al. (2011) (the so-called concurrent “MODIS-era” approach) uses an unsupervised classifier to
222 cluster the individual scene-based multi-spectral Landsat data into ten to fifteen clusters, with the
223 assumption that each cluster in the scene has similar instantaneous anisotropy features. The
224 cluster map is reprojected from UTM to the MODIS sinusoidal projection and MODIS
225 representative pixels that are relatively homogenous on the Landsat scale are identified. The ratio
226 of the albedo-to-reflectance generated from the representative MODIS pixels BRDF which are
227 associated with each Landsat cluster is then calculated to derive a Landsat albedo from the
228 Landsat near nadir reflectance (at view angles $\pm 7.5^\circ$ from nadir) using equation (1).

$$A = (a/r(\Omega_l)) \cdot r_l \quad (1)$$

229 Where A is Landsat albedo to be calculated, r_l is observed Landsat reflectance and Ω_l is viewing
230 and solar geometry of Landsat data. a is albedo and $r(\Omega_l)$ is the reflectance at Landsat sun view
231 geometry. Both a and $r(\Omega_l)$ are derived by the BRDF parameters.

232

233 The cloud-free blue-sky shortwave broadband albedo (the actual bi-hemispherical reflectance) is
234 derived by combining the synthetic shortwave Black-Sky Albedo (BSA) at local solar noon and
235 the White-Sky Albedo (WSA) with a consideration of the diffuse and direct incident radiation at
236 a specific time (Eq. 2) (Lewis and Barnsley, 1994; Román et al., 2010).

237

$$238 \quad \alpha_{blue-sky}(\theta_i) = f_{diffuse}(\theta_i)\alpha_{white-sky} + (1 - f_{diffuse}(\theta_i))\alpha_{black-sky}(\theta_i) \quad (2)$$

239

240 Where $f_{diffuse}(\theta_i)$ is the proportion of diffuse irradiation at a specific solar zenith angle θ_i ; the
241 $f_{diffuse}$ is derived from AOD acquired from the MODIS aerosol product (MOD08).

242

243 Compared to the Normalized Difference Vegetation Index (NDVI) which can become saturated
244 in dense vegetation, the Enhanced Vegetation Index (EVI) (Huete et al., 2002) improves
245 sensitivity in high biomass regions and is used to derive the MODIS phenology product (Zhang
246 et al., 2003). As such, the NBAR-derived EVI time series data are used to detect vegetation
247 phenology metrics in this study.

248

249 **2.3 The synthetic time series of shortwave broadband albedo and vegetation index**

250

251 The STARFM algorithm is used to derive the synthetic time series of daily albedo and enhanced
252 vegetation index at a 30m spatial resolution. STARFM blends the Landsat and MODIS data by
253 using the spatially and temporally weighted difference between paired MODIS and Landsat
254 pixels from same day images to predict intermediate values on MODIS dates and create a
255 comprehensive phenological record (Gao et al., 2006). In this study both the synthetic daily
256 shortwave broadband albedo and the EVI values were generated utilizing STARFM from the
257 paired images of Landsat and MODIS albedo and the paired images of NBAR-derived EVI to
258 model the non-linear change over the entire period (Emelyanova et al., 2013). STARFM is
259 applied directly to the shortwave broadband albedo and EVI values rather than the underlying
260 surface reflectance in order to reduce the mismatch in bandwidths between the Landsat and
261 MODIS data. The daily MODIS NBAR-derived EVI (Collection V006) and Landsat EVI are
262 fused to build EVI time-series for deriving the vegetation phenology. Daily 30 m spatial

263 resolution STARFM images were generated for the entire year of 2007 at Harvard Forest, Santa
 264 Rita in 2011 and Walker Branch in 2005. The spatial extent of STARFM images is 16 km by 14
 265 km at Harvard Forest and 5 km by 5 km at both the Santa Rita and Walker Branch sites. To
 266 facilitate a more robust analysis of the surface heterogeneity, a larger plot was selected for
 267 statistics at the Harvard Forest site (16 km by 14 km). This was done to include most of land
 268 classes of typical forested areas of the northeastern United States (evergreen forest, deciduous
 269 forest, grassland, inland water bodies and residential areas). The cloud, cloud shadow and snow
 270 flags created by the LEDAPS algorithm were applied to select clear sky snow-free Landsat 5 TM
 271 images prior to processing in STARFM (Table 2).

272

273 The phenology metrics (e.g. onset of vegetation green-up) were retrieved by applying the
 274 piecewise logistic function to the synthetic time series snow-free daily EVI (Zhang et al., 2003).
 275 No further smoothing processes was performed over the synthetic time series data before fitting
 276 the piecewise logistic function.

277

278 Table 2. The acquisition dates of Landsat 5 TM images used for the Harvard Forest, Walker
 279 Branch, and Santa Rita sites

Site	Harvard Forest (year-month-day)	Walker Branch (year-month-day)	Santa Rita (year-month-day)
Landsat 5 TM Data	2007-02-11	2005-02-22	2011-01-13
	2007-03-30	2005-03-10	2011-01-29
	2008-04-18*	2005-05-13	2011-02-14
	2007-06-19	2005-09-18	2011-03-02
	2007-09-07	2005-10-04	2011-03-18
		2005-10-20	2011-04-03
			2011-05-21
			2011-06-22
			2011-10-12
			2011-10-28

280

281 * Landsat obtained from 2008-04-18 is utilized for the spring period as there was no available
 282 cloud free imagery in 2007 and no disturbance/change between year 2007 and 2008.

283

284 2.4 Surface heterogeneity analysis

285

286 The heterogeneity of the Enhanced Vegetation Index (EVI) and shortwave broadband blue sky
 287 albedo is analyzed by considering the standard deviation (Eq. 3) and difference between the

288 maximum and minimum values (Eq. 4) within the moderate grid (480 m) using the 30 m
 289 STARFM synthetic datasets. Recognizing that the actual grid size of the so-called “500 m”
 290 MODIS gridded product is 463 m, in this study the analysis is performed for each 480 m grid (16
 291 by 16 Landsat pixels) within the subsets of the three sites.

$$293 \quad Y_{480m-stdv} = \sqrt{(\sum_{i=1}^N (\bar{x}_{30m} - x_{i30m})^2) / (N - 1)} \quad (3)$$

$$295 \quad Y_{480m-diff} = x_{\max(30m)} - x_{\min(30m)} \quad (4)$$

$$297 \quad \bar{Z}_{480m} = (\sum_{j=1}^M Y_{j480m}) / M \quad (5)$$

298
 299 Where x refers to vegetation index or shortwave broadband blue sky albedo at 30 m spatial
 300 resolution. N is the total number of 30 m clear sky pixels within each 480 m grid. M is the
 301 number of 480 m grids within the study area. $Y_{480m-stdv}$ and $Y_{480m-diff}$ are the standard deviation
 302 and difference of the maximum and minimum values within the 480m grid respectively. \bar{Z}_{480m} is
 303 the mean value of standard deviation ($Y_{480m-stdv}$) or difference of maximum and minimum (Y_{480m-}
 304 $diff$) values within the study area. These measures reflect the degrees of heterogeneity within a
 305 MODIS pixel from Landsat pixel resolution

306
 307 The heterogeneity and spatial representativeness of the NEON sites were also analyzed using a
 308 semivariogram analysis (Carroll and Cressie, 1996; Matheron, 1963). The semivariogram is one
 309 of the most efficient tools to reveal the spatial variability of land surfaces and describe the
 310 surface heterogeneity and spatial representativeness (Román et al., 2009; Woodcock et al.,
 311 1988a, 1988b). Albedo spatial representativeness analysis was performed using semivariograms
 312 created from the 30 m Landsat data to evaluate the surface heterogeneity of the regions around
 313 the 20 NEON core ground towers (Román et al., 2009; Wang et al., 2014, 2012). The spatial
 314 representativeness of the ground measurements for moderate spatial resolution satellite products
 315 (e.g. MODIS, VIIRS) is evaluated at each NEON site. Although gridded as a 500 m product, the
 316 MCD43A BRDF/albedo/NBAR products are generated from multi-angular surface reflectance
 317 observations with varied footprints. As such, it is difficult to determine the exact footprint of one
 318 MODIS gridded albedo pixel. Campagnolo et al. (2016) showed that the effective spatial

319 resolution of 500 m gridded MODIS BRDF/albedo/ NBAR product at mid latitudes is around
 320 833 m by 618 m. Therefore, we analyzed the spatial representativeness of each site based on a
 321 conservatively larger area. The ground measurements can be used to appropriately evaluate
 322 moderate spatial resolution remote sensing products if the surface is spatially homogenous within
 323 the larger area. The variogram estimator is fitted to a spherical model to derive spatial attributes
 324 (range, sill and nugget effect). The scale requirement index (R_{se}) (Eq. 6) (Román et al., 2009)
 325 derived from the semivariogram analysis measures the relative spatial variation in albedo
 326 considering both the footprint of the ground instrument and the surrounding landscape. The
 327 surface is spatially representative with respect to the MODIS footprint when the R_{se} is less than
 328 0.243 (Román et al., 2009).

$$329 \quad R_{se} = \exp\left[-\sqrt{(g/a_x)^2 + (g/a_{1.5x})^2}\right]; x = 1.0km \quad (6)$$

330 Where:

$$331 \quad g = 2H\tan(FOV) \quad (7)$$

332 a is the range of two Landsat subsets of sizes x and $1.5x$; H is the height of the field albedometer;
 333 FOV [degrees] is the half field-of-view of the albedometer; g is the footprint of ground albedo
 334 measurements. The site is spatially representative when $g \geq a_x$ and $g \geq a_{1.5x}$. so that the R_{se}
 335 values are between $[0.0, e^{-\sqrt{2}} \approx 0.243]$.

336

337 The sill is the ordinate value of the range at which the variogram levels off to an asymptote and
 338 describes the maximum semivariance. Smaller sill values indicate less variation in albedo and a
 339 more homogenous surface. Note that the spatially representative analysis is only applicable to
 340 moderate resolution satellite measurements such as albedo and in no way reflects the suitability
 341 of the site as a flux tower. Spatially representative analysis is not necessarily required to validate
 342 fine spatial resolution satellite products (e.g. Landsat) as the footprints of the tower
 343 measurements are larger than the Landsat pixel size.

344

345 **3. Results and Discussion**

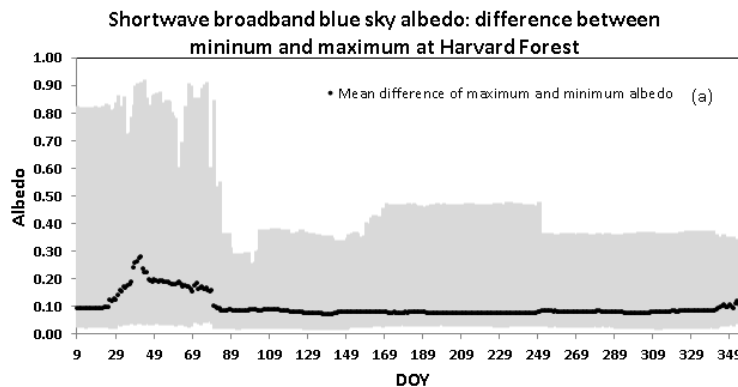
346 **3.1 Land surface heterogeneity**

347

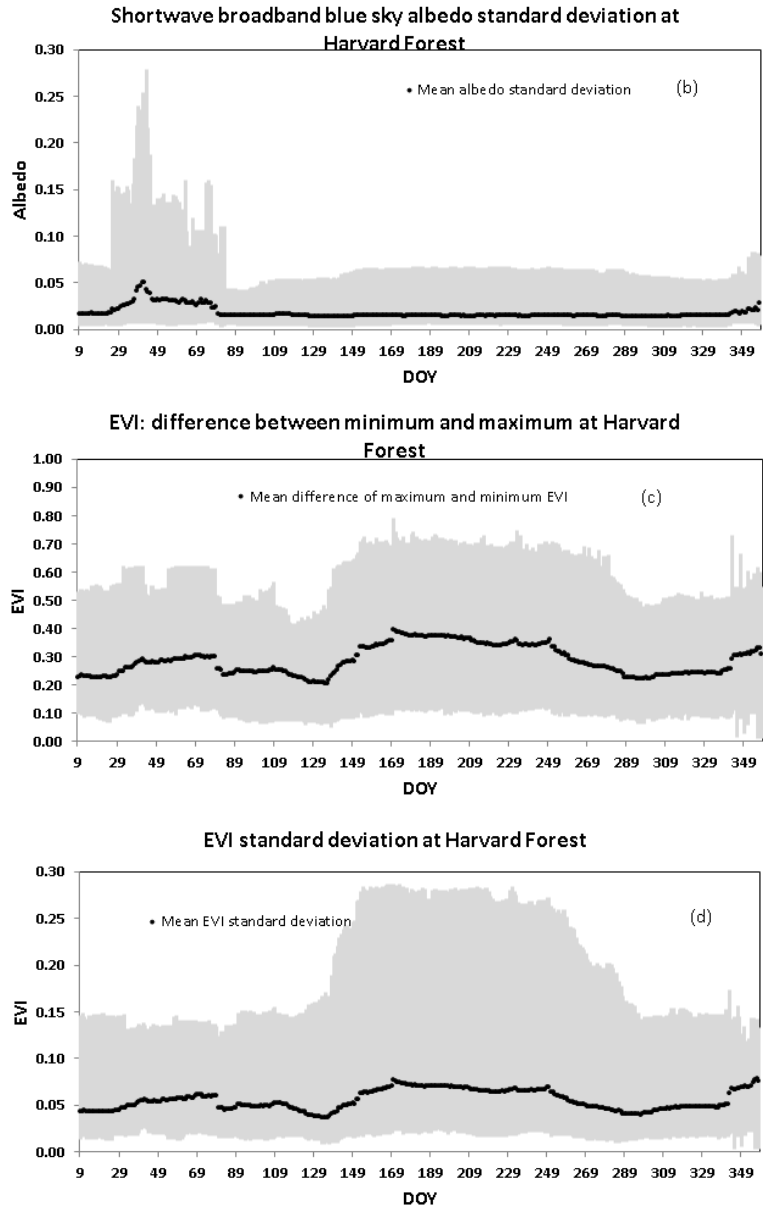
348 The temporal standard deviation and difference of maximum and minimum shortwave
 349 broadband blue sky albedo and EVI over a 16 km by 14 km area at the Harvard Forest site

350 computed using Eq. (1-4) is shown in Fig. 2. The spatial extent of this subset is the same as that
 351 shown in Fig. 5 with the Ameriflux flux tower located at the center. The land cover of this area
 352 includes evergreen forest, deciduous forest, grassland, several inland water bodies and residential
 353 areas. As shown in Fig. 2, albedo is more heterogeneous during the snow-covered period with
 354 the highest albedo values over completely snow-covered surfaces and relatively low albedo over
 355 the forested areas where complete snow cover is rare. The maximum albedo within the study
 356 area is 0.9 while the minimum albedo is less than 0.1. The mean of the difference between
 357 maximum and minimum albedo over the entire study area is around 0.2 during the snow-covered
 358 period and reduced to around 0.1 during the snow-free period. The standard deviation of the
 359 albedo measurements shows similar trends to the mean of the difference between maximum and
 360 minimum albedo. The mean albedo standard deviation is at around 0.014 during the snow-free
 361 period and increases to 0.05 during the snow-covered period. EVI is relatively homogeneous
 362 during the dormant period and more heterogeneous during the growing season due to the
 363 different land cover growth patterns. The mean of the difference between maximum and
 364 minimum EVI over the study area is around 0.35 during the growing season; which is about 0.1
 365 higher than the dormant period. The mean EVI standard deviation during the growing season is
 366 about 0.02 higher than the values during the dormant period.

367



368



369

370

371

372

373

374

375

376

377

378

379

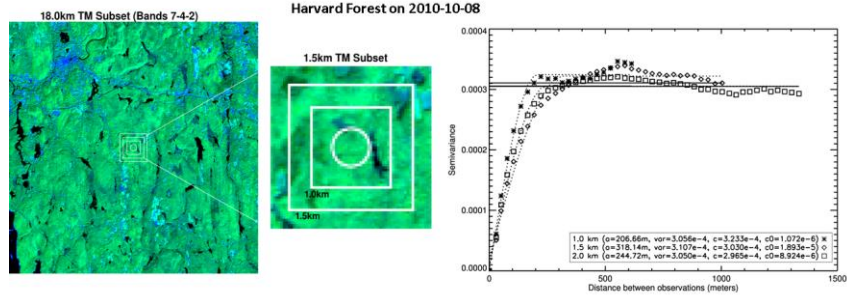
Fig. 2. Temporal plot showing the difference of the maximum and minimum (a) and the standard deviation (b) of shortwave broadband blue sky albedo within the 480 m spatial resolution grids based on 30 m synthetic albedo times series at the Harvard Forest in 2007; Temporal plot of the difference of the maximum and minimum (c) and the standard deviation (d) of EVI within 480 m spatial resolution pixels based on 30 m synthetic EVI time series at the Harvard Forest in 2007. The subset area is 16 km by 14 km. The gray area represents the range of maximum and minimum values within the study area.

380 The big ranges in the standard deviation and maximum and minimum difference of both albedo
381 and EVI indicate that there is significant spatial variation in the land surface of the Harvard
382 Forest at MODIS pixel scales. Therefore, fine spatial resolution data is required to accurately
383 quantify the effects of vegetation changes on the terrestrial carbon cycle and climate change at
384 the patch-scale (Goward et al., 2008; Masek et al., 2013; Shuai et al., 2011).

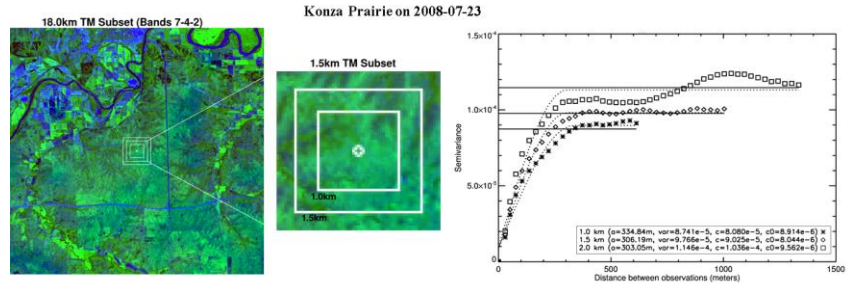
385

386 Here we investigate the representativeness of the albedos that will be measured from NEON
387 towers for the validation of the MODIS albedo product based on the surface heterogeneity and
388 spatial representativeness analysis (Fig. 3). While this analysis focuses on the MODIS albedo
389 product, the results are applicable to other satellite products with similar spatial resolutions (e.g.
390 VIIRS). Most of the NEON core terrestrial sites with tower height higher than 10m are relatively
391 homogenous and the ground measured albedo is spatially representative of the MODIS albedo
392 during both the leaf-on and leaf-off seasons (Table 3). Although the R_{se} values of all the 8 m
393 tower sites are larger than 0.243, the sill values of Konza Prairie Biological Station, Central
394 Plains Experimental Range, Santa Rita Experimental Range, Toolik Lake and 20m tower height
395 Guanica Forest, Yellowstone Northern Range and Upper Waiakea Forest Reserve sites are low at
396 less than 0.0005. These sites can also be considered homogenous and representative. Fig. 4
397 shows that the difference between MODIS and ground measured albedo at the Santa Rita site is
398 less than 0.02. The Caribou Creek taiga, Woodworth, LBJ National Grassland, and Niwot Ridge
399 Mountain Research Station sites represent grassland and forest ecotones and are particularly
400 heterogeneous and may not serve as ideal validation sites for moderate resolution satellite
401 products. In general, shrub and open woodland sites, located in areas with little human activity
402 and no water bodies nearby, are all spatially representative. It should be noted that just as the
403 location of the NEON core towers has been optimized for flux measurements, the actual height
404 of the towers and the placement of the downward radiometers has also been optimized for flux
405 measurements and is governed by the height of the surrounding canopy. Although sites located
406 in heterogenous regions (e.g. the Caribou Creek taiga) are not spatially representative for
407 moderate spatial resolution albedo validation, the footprints of these tower albedo are typically
408 larger than a single pixel of high spatial resolution albedo (e.g. Landsat, Sentinel 2). As such,
409 these sites can still be used to evaluate the accuracy of higher spatial resolution albedo products.

410



411



412

413

414

415

416

417

418

419

420

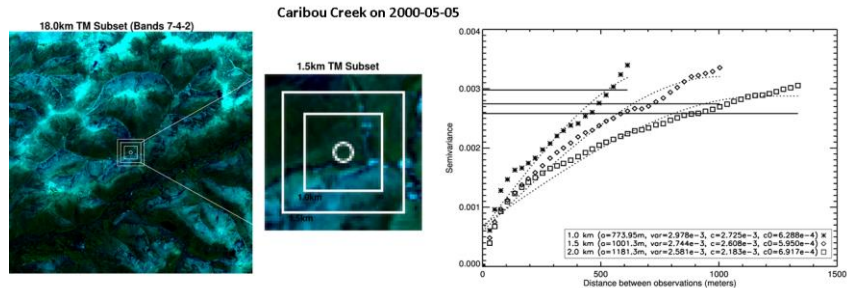
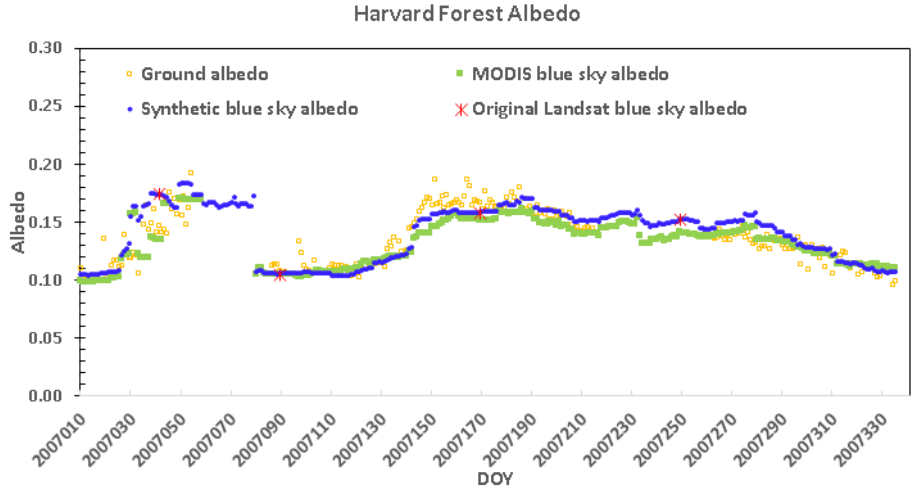
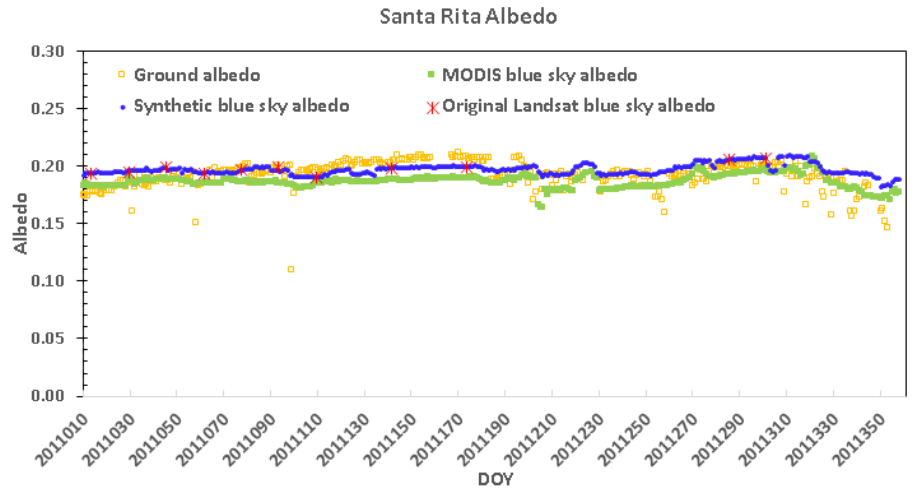


Fig. 3 Shortwave reflectance composite (TM Bands 7–4–2) and corresponding semivariogram functions, variogram estimator (points), spherical model (dotted curves), and sample variance (solid straight lines) using regions of 1.0 km (asterisks), 1.5 km (diamonds), and 2.0 km (squares), centered over Harvard Forest on 2010-10-08, Konza Prairie on 2008-07-23, Caribou Creek - Poker Flats Watershed on 2000-05-05. The circles show the footprint of tower albedo measurements calculated from the tower height and albedometer FOV.

421



422



423

424

425

426

427

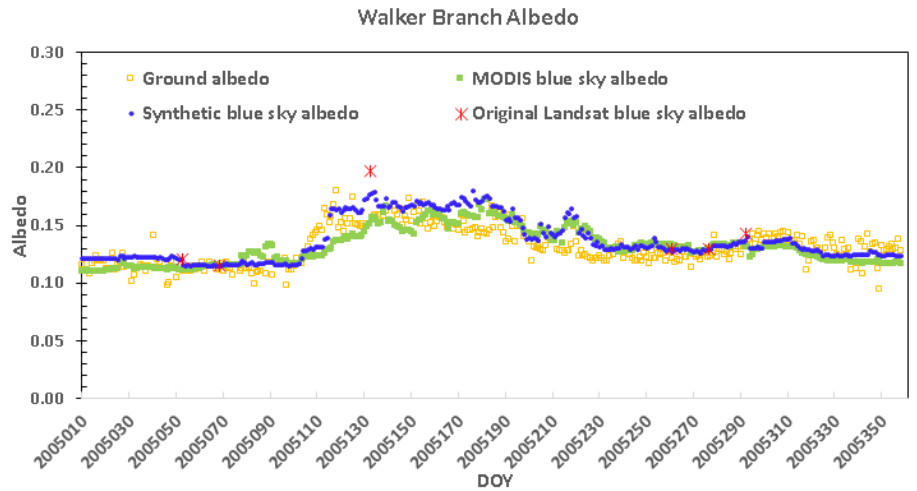


Fig. 4. Comparison of synthetic time series of blue-sky albedo with ground-measured albedo, MODIS blue-sky albedo, and Landsat blue-sky albedo over Harvard Forest (2007), Santa Rita (2011), and Walker Branch (2005) sites. Synthetic, ground-measured,

428 and MODIS albedo measurements were obtained on a daily basis. Landsat 5
 429 measurements were derived from all cloud-free images available in each year (Table 2)

430 Table 3. Spatial representativeness status of NEON sites for moderate spatial resolution satellite
 431 albedo product validation. The highest “sill” values of the three analyzed spatial regions sites
 432 (1.0 km, 1.5 km and 2.0 km) in the semivariogram analysis are presented here.

Domain Number	Site Name	R _{se}		Sill	
		Leaf on	Leaf off	Leaf on	Leaf off
D01	Harvard Forest	0.0726	0.2104	0.0003	0.0003
D02	Smithsonian Conservation Biology Institute	0.0148	0.0253	0.0001	0.0002
D03	Ordway-Swisher Biological Station	0.0618	N/A [§]	0.0003	N/A
D04	Guanica Forest	0.2705	N/A	0.0001	N/A
D05	University of Notre Dame Environmental Research Center	0.1408	0.0673	0.0011	0.0004
D06	Konza Prairie Biological Station	0.6395	0.6531	0.0001	0.0005
D07	Oak Ridge	0.0469	0.1777	0.0003	0.0006
D08	Talladega National Forest	0.0341	N/A	0.0001	N/A
D09	Woodworth	0.5626	0.5738	0.0014	0.0011
D10	Central Plains Experimental Range	N/A	N/A	0.0002	0.0002
D11	LBJ National Grassland	N/A	N/A	0.0005	0.0015
D12	Yellowstone Northern Range (Frog Rock)	0.5222	0.5209	0.0004	0.0004
D13	Niwot Ridge Mountain Research Station	0.5970	0.7196	0.0004	0.0011
D14	Santa Rita Experimental Range	N/A	N/A	0.0002	0.0002
D15	Onaqui-Ault	0.5873	0.5365	0.0001	0.0002

D16	Wind River Experimental Forest	0.0085	N/A	0.0007	N/A
D17	San Joaquin Experimental Range	0.0393	0.0636	0.0001	0.0003
D18	Toolik Lake	N/A	N/A	0.0002	
D19	Caribou Creek - Poker Flats Watershed	N/A	N/A	0.0008	0.0034
D20	Upper Waiakea Forest Reserve	0.4609	N/A	0.0001	N/A

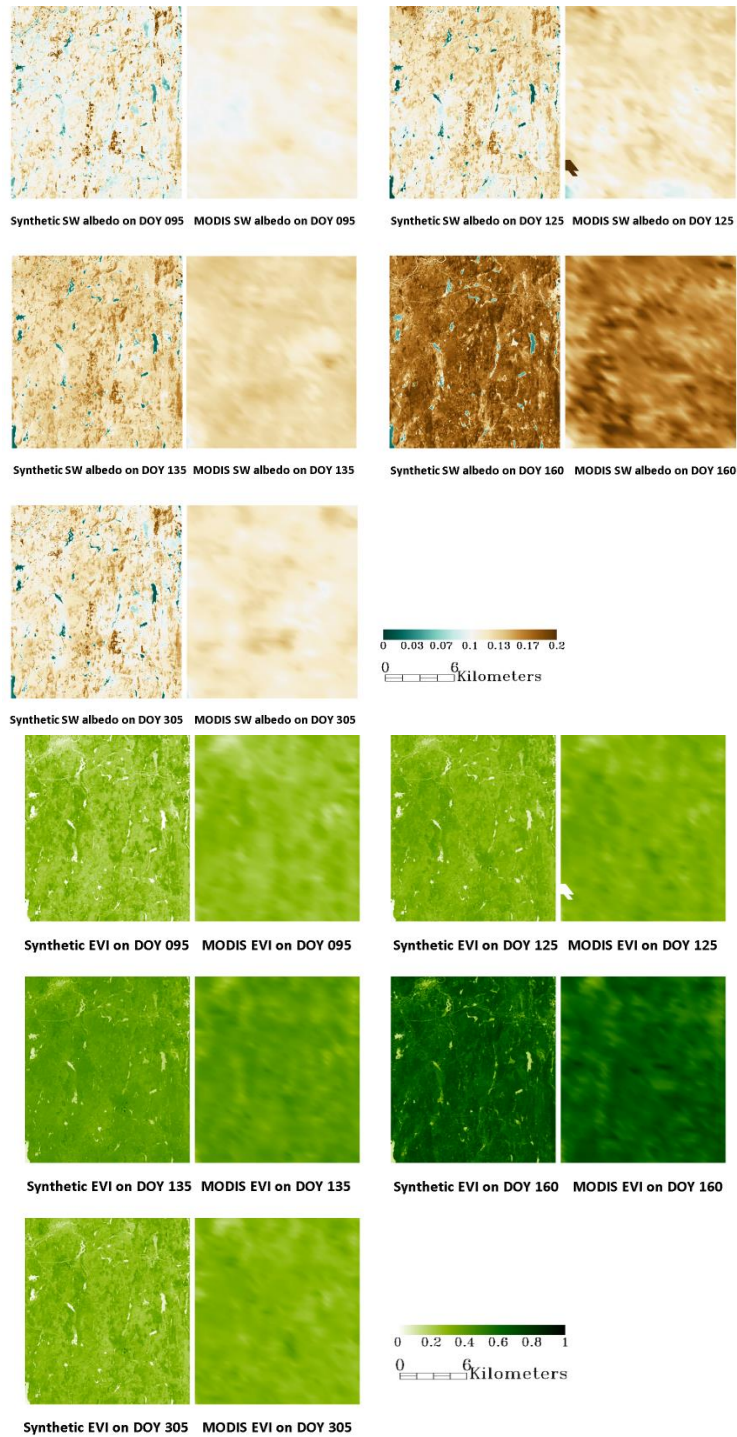
433 [§]N/A represents data not available (evergreen vegetation sites for leaf off (site 3, 4, 16, 19, and
434 20), no clear sky images available (site 8), or sites where the semivariogram curve fails to fit the
435 spherical model (site 10, 11, 14, 18, and 19)).

436 **3.2 Synthetic shortwave albedo and EVI for land surface dynamics monitoring**

437 The synthetic times series of 30 m broadband shortwave blue sky albedo is averaged according
438 to the footprint of the tower albedometer for comparison with ground measurements. The
439 albedos at Harvard Forest are around 0.19 during winter as snow beneath the forest canopy
440 increases reflectance. The albedo decreases with the snowmelt and then increases to a maximum
441 of about 0.16 during the course of the growing season (Fig. 4). Gaps in the data record are a
442 result of missing ground albedo measurements from DOY 55 to 84 at the Harvard forest tower.
443 The MODIS and synthetic albedo were not retrieved from around the Harvard Forest tower from
444 DOY 59 to 79 due to the lack of valid MODIS reflectance data. Unsurprisingly, the synthetic 30
445 m albedo time series captures finer spatial characteristics than the MODIS data alone while
446 maintaining similar seasonal dynamics (Fig. 5). The Santa Rita site is relatively stable with
447 albedos remaining near 0.2 all year (appropriate for such a semiarid open shrub land site). The
448 seasonal dynamics at this site are mainly dominated by the change of soil moisture (Sanchez-
449 Mejia et al., 2014). Walker Branch is a deciduous forest site with no winter snow cover. As such,
450 the albedo is lower than Harvard Forest in the winter (~0.12) and increases to a maximum of
451 0.17 during the growing season. The RMSEs of the synthetic blue sky albedo as compared to the
452 tower albedo values are 0.013, 0.009 and 0.012 for the Harvard Forest, Santa Rita and Walker
453 Branch sites respectively and the biases for the three sites are 0.002, 0.003 and 0.006
454 respectively. The footprint of the tower albedo measurements is close (Santa Rita) to or larger
455 than (Harvard Forest and Walker Branch) the 30 m Landsat and synthetic albedo pixel sizes, yet

456 smaller than the effective spatial resolution of MODIS albedo. Landsat and synthetic albedo
457 values were averaged according to the tower footprints for comparison, as such the area
458 mismatch between combined Landsat and synthetic pixels and the ground footprint is less than
459 the mismatch between ground footprint and a MODIS pixel. As a result, the Landsat and
460 synthetic albedo values are slightly closer to the tower albedos than the MODIS albedo values
461 (Fig. 4) over the three sites. The RMSE of the more homogenous shrub land (Santa Rita) is lower
462 than the values at forest sites (Harvard Forest and Walker Branch). The combined accuracy of
463 the synthetic blue sky albedo at these all three sites (RMSE 0.016, bias -0.013) is close to the
464 values in Shuai et al. (2011) and meets the absolute accuracy requirement of 0.02–0.05 (Sellers
465 et al., 1995) required by modelers. The accuracy of the synthetic time series of blue sky albedo
466 values is affected by the number and quality of the finer spatial resolution data. For example,
467 only one Landsat image is available during the growing season (2005-05-13) at Walker Branch
468 and this Landsat albedo value is 0.04 higher than the measured ground albedo. This observation
469 is close to the edge of a cloud and is potentially contaminated by a thin cloud not detected with
470 the Landsat cloud mask. Enhanced temporal resolution coverage of finer scale satellite data over
471 these sites would obviously improve the synthetic time series results. The availability and
472 improved technical capabilities (1.38 μm cirrus band and the improved radiometric resolution) of
473 Landsat 8 (2013) and Sentinel-2A (2015) obviously will contribute significantly to improved fine
474 scale synthetic time series results. The synthetic 30 m albedo show a wider data range than the
475 stand-alone MODIS albedo. This is because spatial details captured at the Landsat 30 m
476 resolution are mixed/smoothed at the MODIS 500 m resolution. However, the number of original
477 clear sky Landsat 5 observations is very limited at the Harvard Forest and Walker Branch sites
478 with only four at Harvard Forest in 2007 and six at Walker Branch in 2005. The Santa Rita site,
479 in a semiarid area, had 11 original clear sky Landsat 5 observations in 2011 (Table 2). However,
480 in all cases, the daily synthetic EVI and albedo time series significantly expand the spatial and
481 temporal resolution of datasets for climate study.

482



483

484
 485
 486
 487
 488
 489
 490

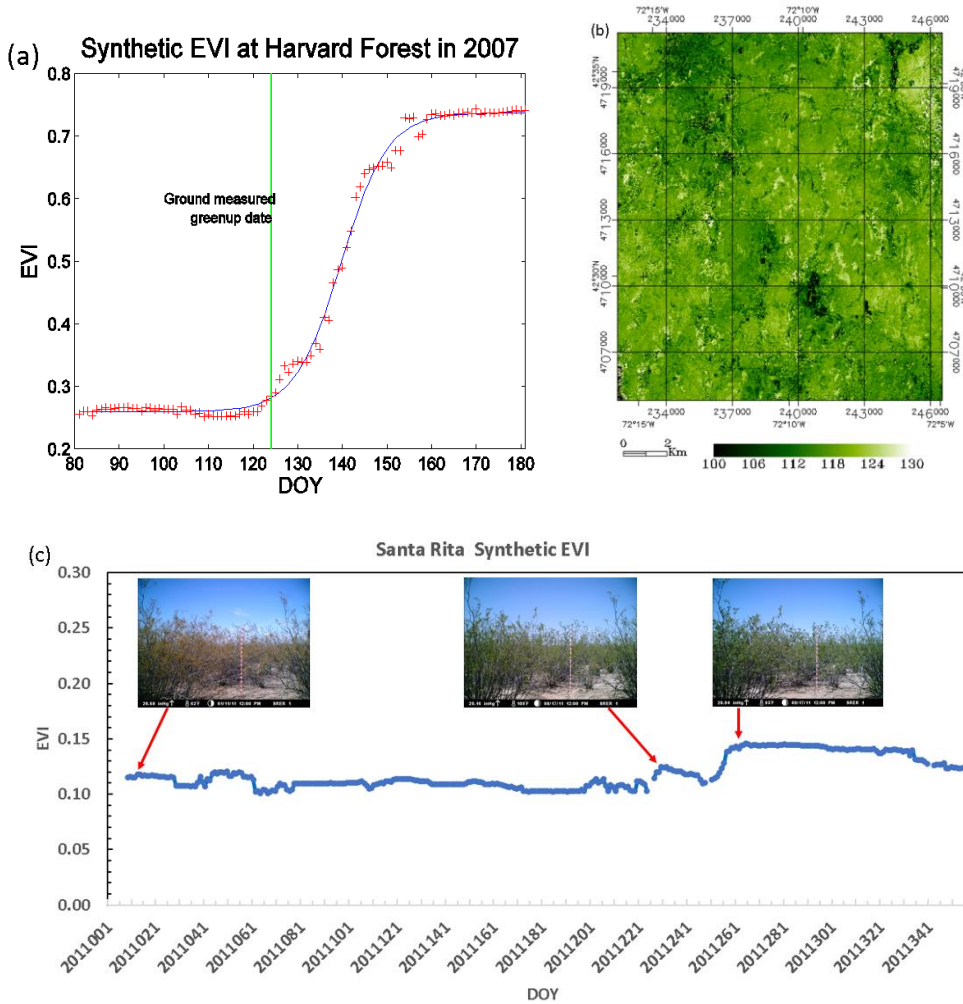
Fig. 5. The synthetic time series and MODIS shortwave broadband blue sky albedo and EVI at Harvard Forest subset (16 km by 14 km) on DOY 95, 125, 135, 160 and 305 in 2007.

491 The phenological metrics derived from multi-day composite datasets can mask high-frequency
492 vegetation changes (Ju et al., 2010; McKellip et al., 2005; Narasimhan and Stow, 2010). Shuai et
493 al. (2013) showed that subtle details in growth stages can be captured from daily MODIS
494 NBAR-derived EVI. Currently the temporal resolution of the Landsat data makes it difficult to
495 capture vegetation phenological metrics, particularly in the shoulder seasons (e.g. green-up,
496 senescence) which are important in analyzing the impacts of climate change. The MODIS-
497 Landsat derived synthetic daily 30 m spatial resolution times series of EVI can be used to
498 monitor complex land surface characteristics, especially rapidly changing seasonal dynamics.
499 The phenology patterns of the vegetation were well captured by the synthetic EVI time series at
500 Harvard Forest in 2007 (Fig. 5; Fig. 6). The logistic model fitted EVI dates agrees well with the
501 synthetic temporal EVI dates. The ground phenology information at Harvard Forest was
502 measured every 4 days during the green-up period. In 2007, the green-up date determined from
503 the synthetic 30 m data sets (Day Of Year (DOY) 120) matches well with the field measured
504 date (124). The green-up date derived from 500 m MODIS product (MCD12Q2) (Zhang et al.,
505 2003) was considerably earlier at DOY 115. The difference in the onset of green-up within a
506 single MODIS pixel can be more than 10 days over the same forest type (Fig. 6b). This spatial
507 variation in phenology could be caused by species distribution or small scale microclimates.
508 Small scale microclimates have previously been shown to result in large phenological variability
509 within hundreds of meters (Klosterman et al., 2014; Vitasse et al., 2009). The temporal variation
510 of synthetic EVI times series however, captures the development of foliage stages at the Santa
511 Rita site (Fig. 6c). The shrubs started to green-up on DOY 220 and reached the first peak on
512 DOY 230 and the second peak on DOY 260 in 2011. The single year analysis in this study
513 demonstrate an ability to derive temporal vegetation variations at high spatial resolution using a
514 variety of data fusion techniques. Further work is required for different vegetation types over a
515 longer period to extend this study to completely assess the implication of land surface
516 heterogeneity on the phenological analyses.

517

518 The synthetic EVI also shows greater spatial detail than the MODIS EVI, especially over more
519 heterogeneous surfaces. This improves our ability to characterize spatial variations in EVI across
520 species and communities. The maximum EVI standard deviation within a 480 m grid at Harvard
521 Forest is over 0.25 and the difference of maximum and minimum EVI within the 480 m grid can

522 be as high as 0.7 during the growing season (Fig. 2). In addition, the boundaries between forest
 523 types and water bodies are very clear in the synthetic EVI but difficult to identify in the MODIS
 524 EVI.
 525



526
 527

528
 529

530 Fig. 6. (a) Temporal plot of synthetic time series EVI (red +) and logistic model fit (blue line) at
 531 Harvard Forest flux tower in 2007, (b) the onset (DOY) of green-up at Harvard Forest subset (16
 532 km by 14 km) and (c) the temporal plot of synthetic EVI and phenocam photos at Santa Rita site.
 533

534 4. Conclusion

535

536 The MODIS-Landsat coupled synthetic albedo and EVI times series are able to capture the land
 537 surface dynamics at high spatial resolution. Such a capability lays the ground work for long-
 538 term monitoring of vegetation phenology at the stand scale in response to climate change,

539 disturbance regimes, and other drivers. The heterogeneity analyses of all of the NEON sites and
540 of the three Ameriflux sites used in this study indicates that the range of EVI and albedo within
541 moderate spatial resolution grids is very large and higher spatial resolution vegetation index and
542 albedo values are necessary to understand how individual vegetation types are responding to
543 environmental forcing. The daily high spatial resolution synthetic vegetation index time series
544 enhances the monitoring of vegetation phenology change. At the Harvard Forest site, the
545 difference between the synthetic EVI determinations and the ground measured green-up date is
546 within 4 days. This suggests that over mixed deciduous broadleaf and evergreen needleleaf forest
547 ecosystems, the modeled phenology can be used to capture vegetation temporal variations at the
548 landscape scale. The synthetic albedo time series match well with the ground albedo values with
549 RMSE and bias less than 0.013 and within ± 0.006 respectively over the three Ameriflux sites.
550 As more of the spatially representative NEON core site towers are established, continued
551 comparisons and validation can be done to monitor seasonal and temporal trends. The
552 establishment of the NEON core sites will contribute significantly to our knowledge of a
553 diversity of ecosystems and provide key validation measurements for both satellite data and
554 future models and simulations. However, as noted, the NEON sites were originally selected for
555 applicability to serve as flux sites and not necessarily the best placements to evaluate satellite
556 products, and therefore, this analysis of spatial representativeness is important in defining the
557 appropriate usage of these NEON data. The observations of higher resolution surface phenology
558 and energy change from the synthetic time series data will be continued with the newer
559 generation of satellites including Landsat 8 Operational Land Imager (OLI), Sentinel-2A/B
560 MultiSpectral Instrument (MSI), and Suomi-NPP Visible Infrared Imager Radiometer Suite
561 (VIIRS) satellite sensors.

562

563 **Acknowledgement**

564

565 The Landsat data were downloaded from the USGS Earth Resources Observation and Science
566 (EROS) Center Science Processing Architecture (ESPA) (<https://espa.cr.usgs.gov>). MODIS data
567 were obtained from the NASA's Earth Observing System Data and Information System
568 (EOSDIS) (<http://reverb.echo.nasa.gov>). Field albedo measurements were downloaded from
569 AmeriFlux website (<http://ameriflux.lbl.gov/>). We gratefully acknowledge Dr. Tilden Meyers

570 from NOAA for providing ground albedo measurements at Walker Branch site, Dr. David
571 Fitzjarrald from State University of New York at Albany for providing Harvard Forest ground
572 albedo measurements and John O'Keefe from Harvard University for providing ground measured
573 phenology data at Harvard Forest. This research was supported by NASA award [grant number
574 NNX14A173G], Harvard Forest NSF LTER grant [grant number DEB-1237491] and NSF
575 CAREER Award [grant number EAR-1255013]. Any use of trade, product, or firm names is for
576 descriptive purposes only and does not imply endorsement by the U.S. Government.

577

578 **Reference:**

579

- 580 Baldocchi, D., Falge, E., Wilson, K., 2001. A spectral analysis of biosphere – atmosphere trace
581 gas flux densities and meteorological variables across hour to multi-year time scales. *Agric.*
582 *For. Meteorol.* 107, 1–27. doi:10.1016/S0168-1923(00)00228-8
- 583 Campagnolo, M.L., Sun, Q., Liu, Y., Schaaf, C., Wang, Z., Román, M.O., 2016. Estimating the
584 effective spatial resolution of the operational BRDF, albedo, and nadir reflectance products
585 from MODIS and VIIRS. *Remote Sens. Environ.* 175, 52–64. doi:10.1016/j.rse.2015.12.033
- 586 Carroll, S.S., Cressie, N., 1996. A comparison of geostatistical methodologies used to estimate
587 snow water equivalent. *Water Resour. Bull.* 32, 267–278. doi:10.1111/j.1752-
588 1688.1996.tb03450.x
- 589 Churkina, G., Schimel, D., Braswell, B.H., Xiao, X.M., 2005. Spatial analysis of growing season
590 length control over net ecosystem exchange. *Glob. Chang. Biol.*
- 591 Cleland, E.E., Chiariello, N.R., Loarie, S.R., Mooney, H.A., Field, C.B., 2006. Diverse responses
592 of phenology to global changes in a grassland ecosystem. *Proc. Natl. Acad. Sci. U. S. A.*
593 103, 13740–13744.
- 594 Dirmeyer, P.A., Shukla, J., 1994. Albedo as a modulator of climate response to tropical
595 deforestation. *J. Geophys. Res.* 99, 20863–20877.
- 596 Emelyanova, I. V., McVicar, T.R., Van Niel, T.G., Li, L.T., van Dijk, A.I.J.M., 2013. Assessing
597 the accuracy of blending Landsat–MODIS surface reflectances in two landscapes with
598 contrasting spatial and temporal dynamics: A framework for algorithm selection. *Remote*
599 *Sens. Environ.* 133, 193–209. doi:10.1016/j.rse.2013.02.007
- 600 Friedl, M. a, Gray, J.M., Melaas, E.K., Richardson, A.D., Hufkens, K., Keenan, T.F., Bailey, A.,
601 O'Keefe, J., 2014. A tale of two springs: using recent climate anomalies to characterize the
602 sensitivity of temperate forest phenology to climate change. *Environ. Res. Lett.* 9, 054006.
603 doi:10.1088/1748-9326/9/5/054006
- 604 Ganguly, S., Friedl, M. a., Tan, B., Zhang, X., Verma, M., 2010. Land surface phenology from
605 MODIS: Characterization of the Collection 5 global land cover dynamics product. *Remote*
606 *Sens. Environ.* 114, 1805–1816. doi:10.1016/j.rse.2010.04.005
- 607 Gao, F., Masek, J., Schwaller, M., Hall, F., 2006. On the blending of the Landsat and MODIS
608 surface reflectance: predicting daily Landsat surface reflectance. *IEEE Trans. Geosci.*
609 *Remote Sens.* 44, 2207–2218. doi:10.1109/TGRS.2006.872081

610 Goward, S.N., Masek, J.G., Cohen, W., Moisen, G., Collatz, G.J., Healey, S., Houghton, R. a.,
611 Huang, C., Kennedy, R., Law, B., Powell, S., Turner, D., Wulder, M. a., 2008. Forest
612 Disturbance and North American Carbon Flux. *Eos, Trans. Am. Geophys. Union* 89, 105.
613 doi:10.1029/2008EO110001

614 Hall, A., 2004. The Role of Surface Albedo Feedback in Climate. *J. Clim.* 17, 1550–1568.
615 doi:10.1175/1520-0442(2004)017<1550:TROSAF>2.0.CO;2

616 Hamilton, M.P., Graham, E. a., Rundel, P.W., Allen, M.F., Kaiser, W., Hansen, M.H., Estrin,
617 D.L., 2007. New Approaches in Embedded Networked Sensing for Terrestrial Ecological
618 Observatories. *Environ. Eng. Sci.* 24, 192–204. doi:10.1089/ees.2006.0045

619 Hansen, J., Ruedy, R., Sato, M., Lo, K., 2010. Global Surface Temperature Change. *Rev.*
620 *Geophys.* 48, 1–29. doi:10.1029/2010RG000345.1.INTRODUCTION

621 Hansen, J., Sato, M., Ruedy, R., Lo, K., Lea, D.W., Medina-elizade, M., 2006. Global
622 temperature change. *Proc. Natl. Acad. Sci. U. S. A.* 103, 14288–14293.

623 He, T., Liang, S., Wang, D., Shuai, Y., Yu, Y., 2014. Fusion of satellite land surface albedo
624 products across scales using a multiresolution tree method in the north central United States.
625 *IEEE Trans. Geosci. Remote Sens.* 52, 3428–3439. doi:10.1109/TGRS.2013.2272935

626 Hilker, T., Wulder, M. a., Coops, N.C., Seitz, N., White, J.C., Gao, F., Masek, J.G., Stenhouse,
627 G., 2009. Generation of dense time series synthetic Landsat data through data blending with
628 MODIS using a spatial and temporal adaptive reflectance fusion model. *Remote Sens.*
629 *Environ.* 113, 1988–1999. doi:10.1016/j.rse.2009.05.011

630 Huete, A., Didan, K., Miura, T., Rodriguez, E.P., Gao, X., Ferreira, L.G., 2002. Overview of the
631 radiometric and biophysical performance of the MODIS vegetation indices. *Remote Sens.*
632 *Environ.* 83, 195–213. doi:10.1016/S0034-4257(02)00096-2

633 Jin, Y., Schaaf, C.B., Gao, F., Li, X., Strahler, A.H., 2003. Consistency of MODIS surface
634 bidirectional reflectance distribution function and albedo retrievals: 1. Algorithm
635 performance. *J. Geophys. Res.* 108.

636 Jin, Y.B.S., Gao, F., Li, X., Strahler, A.H., Zeng, X., Dickinson, R.E., 2002. How does snow
637 impact the albedo of vegetated land surfaces as analyzed with MODIS data? *Geophys. Res.*
638 *Lett.* 29, 12–15. doi:10.1029/2001GL014132

639 Ju, J., Roy, D.P., Shuai, Y., Schaaf, C., 2010. Development of an approach for generation of
640 temporally complete daily nadir MODIS reflectance time series. *Remote Sens. Environ.*
641 114, 1–20. doi:10.1016/j.rse.2009.05.022

642 Kampe, T.U., 2010. NEON: the first continental-scale ecological observatory with airborne
643 remote sensing of vegetation canopy biochemistry and structure. *J. Appl. Remote Sens.* 4,
644 043510. doi:10.1117/1.3361375

645 Keller, M., Schimel, D.S., Hargrove, W.W., Hoffman, F.M., 2008. A continental strategy for the
646 National Ecological Observatory Network. *Front. Ecol. Environ.* 6, 282–284.
647 doi:10.1890/1540-9295(2008)6[282:ACSFTN]2.0.CO;2

648 Klosterman, S.T., Hufkens, K., Gray, J.M., Melaas, E., Sonnentag, O., Lavine, I., Mitchell, L.,
649 Norman, R., Friedl, M.A., Richardson, A.D., 2014. Evaluating remote sensing of deciduous
650 forest phenology at multiple spatial scales using PhenoCam imagery. *Biogeosciences* 11,
651 4305–4320. doi:10.5194/bg-11-4305-2014

- 652 Körner, C., Basler, D., 2010. Phenology Under Global Warming. *Science* (80-.). 327, 1461–
653 1462. doi:10.1126/science.1186473
- 654 Law, B., Falge, E., Gu, L., Baldocchi, D., Bakwin, P., Berbigier, P., Davis, K., Dolman, A., Falk,
655 M., Fuentes, J., 2002. Environmental controls over carbon dioxide and water vapor
656 exchange of terrestrial vegetation. *Agric. For. Meteorol.* 113, 97–120. doi:10.1016/S0168-
657 1923(02)00104-1
- 658 Lewis, P., Barnsley, M., 1994. Influence of the sky radiance distribution on various formulations
659 of the earth surface albedo. *Proc. Conf. Phys. Meas. Signatures Remote Sens.*
- 660 Liang, L., Schwartz, M.D., Wang, Z., Gao, F., Schaaf, C.B., Tan, B., Morisette, J.T., Zhang, X.,
661 2014. A Cross Comparison of Spatiotemporally Enhanced Springtime Phenological
662 Measurements From Satellites and Ground in a Northern U.S. Mixed Forest. *IEEE Trans.*
663 *Geosci. Remote Sens.* 52, 7513–7526. doi:10.1109/TGRS.2014.2313558
- 664 Liang, S., Fang, H., Chen, M., Shuey, C.J., Walthall, C., Daughtry, C., Morisette, J., Schaaf, C.,
665 Strahler, A., 2002. Validating MODIS land surface reflectance and albedo products:
666 methods and preliminary results. *Remote Sens. Environ.* 83, 149–162. doi:10.1016/S0034-
667 4257(02)00092-5
- 668 Liu, J., Schaaf, C., Strahler, A., Jiao, Z., Shuai, Y., Zhang, Q., Roman, M., Augustine, J. a.,
669 Dutton, E.G., 2009. Validation of Moderate Resolution Imaging Spectroradiometer
670 (MODIS) albedo retrieval algorithm: Dependence of albedo on solar zenith angle. *J.*
671 *Geophys. Res.* 114, D01106. doi:10.1029/2008JD009969
- 672 Lofgren, B., 1995. Surface albedo-climate feedback simulated using two-way coupling. *J. Clim.*
673 8, 2543–2562.
- 674 Lucht, W., Schaaf, C.B., Strahler, a. H., 2000. An algorithm for the retrieval of albedo from
675 space using semiempirical BRDF models. *IEEE Trans. Geosci. Remote Sens.* 38, 977–998.
676 doi:10.1109/36.841980
- 677 Masek, J.G., Goward, S.N., Kennedy, R.E., Cohen, W.B., Moisen, G.G., Schleeweis, K., Huang,
678 C., 2013. United States Forest Disturbance Trends Observed Using Landsat Time Series.
679 *Ecosystems* 16, 1087–1104. doi:10.1007/s10021-013-9669-9
- 680 Masek, J.G., Vermote, E.F., Saleous, N.E., Wolfe, R., Hall, F.G., Huemmrich, K.F., Gao, F.,
681 Kutler, J., Lim, T., 2006. A Landsat Surface Reflectance Dataset. *IEEE Geosci. Remote*
682 *Sens. Lett.* 3, 68–72.
- 683 Matheron, G., 1963. Principles of geostatistics. *Econ. Geol.* 58, 1246–1266.
684 doi:10.2113/gsecongeo.58.8.1246
- 685 McKellip, R., Ryan, R.E., Blonski, S., Prados, D., 2005. Crop surveillance demonstration using a
686 near-daily MODIS derived vegetation index time series, in: *Proceedings of the Third*
687 *International Workshop on the Analysis of Multi-Temporal Remote Sensing Images 2005.*
688 pp. 54–58. doi:10.1109/AMTRSI.2005.1469839
- 689 Menzel, A., Fabian, P., 1999. Growing season extended in Europe. *Nature* 397, 659.
690 doi:10.1038/311558a0
- 691 Menzel, A., Sparks, T.H., Estrella, N., Koch, E., Aasa, A., Ahas, R., Alm-Kubler, K., Bissolli, P.,
692 Braslavska, O., Briede, A., Chmielewski, F.M., Crepinsek, Z., Curnel, Y., Dahl, A., Defila,
693 C., Donnelly, A., Filella, Y., Jatczak, K., Mage, F., Mestre, A., Nordli, O., Penuelas, J.,

694 Pirinen, P., Remisova, V., Scheifinger, H., Striz, M., Susnik, A., Viet, V., Arnold, J.H.,
695 Wielgolaski, F.-E., Zach, S., Zust, A., 2006. European phenological response to climate
696 change matches the warming pattern. *Glob. Chang. Biol.* 12, 1969–1976.

697 Myneni, R.B., Keeling, C.D., Tucker, C.J., Asrar, G., Nemani, R.R., 1997. Increased plant
698 growth in the northern high latitudes from 1981 to 1991. *Nature* 386, 698–702.

699 Narasimhan, R., Stow, D., 2010. Daily MODIS products for analyzing early season vegetation
700 dynamics across the North Slope of Alaska. *Remote Sens. Environ.* 114, 1251–1262.
701 doi:10.1016/j.rse.2010.01.017

702 Ollinger, S. V, Richardson, A.D., Martin, M.E., Hollinger, D.Y., Frohling, S.E., Reich, P.B.,
703 Plourde, L.C., Katul, G.G., Munger, J.W., Oren, R., Smith, M.L., Paw U, K.T., Bolstad, P.
704 V, Cook, B.D., Day, M.C., Martin, T.A., Monson, R.K., Schmid, H.P., 2008. Canopy
705 nitrogen, carbon assimilation, and albedo in temperate and boreal forests: Functional
706 relations and potential climate feedbacks. *Proc. Natl. Acad. Sci. U. S. A.* 105, 19336–
707 19341. doi:10.1073/pnas.0810021105

708 Piao, S., Friedlingstein, P., Ciais, P., Viovy, N., Demarty, J., 2007. Growing season extension
709 and its impact on terrestrial carbon cycle in the Northern Hemisphere over the past 2
710 decades. *Global Biogeochem. Cycles* 21, 1–11. doi:10.1029/2006GB002888

711 Privette, J.L., Eck, T.F., Deering, D.W., 1997. Estimating spectral albedo and nadir reflectance
712 through inversion of simple BRDF models with AVHRR/MODIS-like data. *J. Geophys.*
713 *Res.* 102, 29529–29542.

714 Richardson, A.D., Anderson, R.S., Arain, M.A., Barr, A.G., Bohrer, G., Chen, G., Chen, J.M.,
715 Ciais, P., Davis, K.J., Desai, A.R., Dietze, M.C., Dragoni, D., Garrity, S.R., Gough, C.M.,
716 Grant, R., Hollinger, D.Y., Margolis, H. a., McCaughey, H., Migliavacca, M., Monson,
717 R.K., Munger, J.W., Poulter, B., Raczka, B.M., Ricciuto, D.M., Sahoo, A.K., Schaefer, K.,
718 Tian, H., Vargas, R., Verbeeck, H., Xiao, J., Xue, Y., 2012. Terrestrial biosphere models
719 need better representation of vegetation phenology: results from the North American
720 Carbon Program Site Synthesis. *Glob. Chang. Biol.* 18, 566–584. doi:10.1111/j.1365-
721 2486.2011.02562.x

722 Richardson, A.D., Hollinger, D.Y., Dail, D.B., Lee, J.T., Munger, J.W., O’keefe, J., 2009.
723 Influence of spring phenology on seasonal and annual carbon balance in two contrasting
724 New England forests. *Tree Physiol.* 29, 321–331.

725 Richardson, A.D., Keenan, T.F., Migliavacca, M., Ryu, Y., Sonnentag, O., Toomey, M., 2013.
726 Climate change, phenology, and phenological control of vegetation feedbacks to the climate
727 system. *Agric. For. Meteorol.* 169, 156–173. doi:10.1016/j.agrformet.2012.09.012

728 Richardson, A.D., O’Keefe, J., 2009. Phenological differences between understory and overstory
729 a case study using the long-term Harvard Forest records, in: *Phenology of Ecosystem*
730 *Processes: Applications in Global Change Research.* pp. 87–117. doi:10.1007/978-1-4419-
731 0026-5_4

732 Román, M.O., Schaaf, C.B., Lewis, P., Gao, F., Anderson, G.P., Privette, J.L., Strahler, A.H.,
733 Woodcock, C.E., Barnsley, M., 2010. Assessing the coupling between surface albedo
734 derived from MODIS and the fraction of diffuse skylight over spatially-characterized
735 landscapes. *Remote Sens. Environ.* 114, 738–760. doi:10.1016/j.rse.2009.11.014

- 736 Román, M.O., Schaaf, C.B., Woodcock, C.E., Strahler, A.H., Yang, X., Braswell, R.H., Curtis,
737 P.S., Davis, K.J., Dragoni, D., Goulden, M.L., 2009. The MODIS (Collection V005)
738 BRDF/albedo product: Assessment of spatial representativeness over forested landscapes.
739 *Remote Sens. Environ.* 113, 2476–2498. doi:10.1016/j.rse.2009.07.009
- 740 Roy, D.P., Ju, J., Lewis, P., Schaaf, C., Gao, F., Hansen, M., Lindquist, E., 2008. Multi-temporal
741 MODIS–Landsat data fusion for relative radiometric normalization, gap filling, and
742 prediction of Landsat data. *Remote Sens. Environ.* 112, 3112–3130.
743 doi:10.1016/j.rse.2008.03.009
- 744 Running, S.W., Baldocchi, D.D., Turner, D.P., Gower, S.T., Bakwin, P.S., Hibbard, K.A., 1999.
745 A Global Terrestrial Monitoring Network Integrating Tower Fluxes, Flask Sampling,
746 Ecosystem Modeling and EOS Satellite Data. *Remote Sens. Environ.* 70, 108–127.
747 doi:10.1016/S0034-4257(99)00061-9
- 748 Sanchez-Mejia, Z.M., Papuga, S.A., 2014. Observations of a two-layer soil moisture influence
749 on surface energy dynamics and planetary boundary layer characteristics in a semiarid
750 shrubland. *Water Resour. Res.* 50, 306–317. doi:10.1002/2013WR014135
- 751 Sanchez-Mejia, Z.M., Papuga, S.A., Swetish, J.B., Van Leeuwen, W.J.D., Szutu, D., Hartfield,
752 K., 2014. Quantifying the influence of deep soil moisture on ecosystem albedo: The role of
753 vegetation. *Water Resour. Res.* 50, 4038–4053. doi:10.1002/2013WR014150
- 754 Schaaf, C.B., 2008. Albedo and Reflectance Anisotropy, Terrestrial Essential Climate Variables
755 for Climate Change Assessment, Mitigation and Adaptation, in: Sessa, R., Han, D. (Eds.),
756 *GTOS-52*. pp. 28–29.
- 757 Schaaf, C.B., Gao, F., Strahler, A.H., Lucht, W., Li, X., Tsang, T., Strugnell, N.C., Zhang, X.,
758 Jin, Y., Muller, J.-P., Lewis, P., Barnsley, M., Hobson, P., Disney, M., Roberts, G.,
759 Dunderdale, M., Doll, C., d’Entremont, R.P., Hu, B., Liang, S., Privette, J.L., Roy, D.,
760 2002. First operational BRDF, albedo nadir reflectance products from MODIS. *Remote*
761 *Sens. Environ.* 83, 135–148. doi:10.1016/S0034-4257(02)00091-3
- 762 Schaaf, C.B., Liu, J., Gao, F., Strahler, A.H., 2011. MODIS Albedo and Reflectance Anisotropy
763 Products from Aqua and Terra, in: B. Ramachandran, C. Justice, M.A. (Ed.), *Land Remote*
764 *Sensing and Global Environmental Change Remote Sensing and Digital Image Processing*.
765 Springer, pp. 549–561.
- 766 Schimel, D., Hargrove, W., Hoffman, F., MacMahon, J., 2007. NEON: a hierarchically designed
767 national ecological network. *Front. Ecol. Environ.* 5, 59–59. doi:10.1890/1540-
768 9295(2007)5[59:NAHDNE]2.0.CO;2
- 769 Sellers, P.J., Meeson, B.W., Hall, F.G., Asrar, G., Murphy, R.E., Schiffer, R. a., Bretherton, F.P.,
770 Dickinson, R.E., Ellingson, R.G., Field, C.B., Huemmrich, K.F., Justice, C.O., Melack,
771 J.M., Roulet, N.T., Schimel, D.S., Try, P.D., 1995. Remote sensing of the land surface for
772 studies of global change: Models — algorithms — experiments. *Remote Sens. Environ.* 51,
773 3–26. doi:10.1016/0034-4257(94)00061-Q
- 774 Shuai, Y., Masek, J.G., Gao, F., Schaaf, C.B., 2011. An algorithm for the retrieval of 30-m
775 snow-free albedo from Landsat surface reflectance and MODIS BRDF. *Remote Sens.*
776 *Environ.* 115, 2204–2216. doi:10.1016/j.rse.2011.04.019
- 777 Shuai, Y., Masek, J.G., Gao, F., Schaaf, C.B., He, T., 2014. An approach for the long-term 30-m

778 land surface snow-free albedo retrieval from historic Landsat surface reflectance and
779 MODIS-based a priori anisotropy knowledge. *Remote Sens. Environ.* 152, 467–479.
780 doi:10.1016/j.rse.2014.07.009

781 Shuai, Y., Schaaf, C., Zhang, X., Strahler, A., Roy, D., Morisette, J., Wang, Z., Nightingale, J.,
782 Nickeson, J., Richardson, A.D., Xie, D., Wang, J., Li, X., Strabala, K., Davies, J.E., 2013.
783 Daily MODIS 500 m reflectance anisotropy direct broadcast (DB) products for monitoring
784 vegetation phenology dynamics. *Int. J. Remote Sens.* 34, 5997–6016.
785 doi:10.1080/01431161.2013.803169

786 Vitasse, Y., Delzon, S., Dufr ne, E., Pontailier, J.Y., Louvet, J.M., Kremer, A., Michalet, R.,
787 2009. Leaf phenology sensitivity to temperature in European trees: Do within-species
788 populations exhibit similar responses? *Agric. For. Meteorol.* 149, 735–744.
789 doi:10.1016/j.agrformet.2008.10.019

790 Wang, Z., Schaaf, C.B., Chopping, M.J., Strahler, A.H., Wang, J., Rom n, M.O., Rocha, A. V.,
791 Woodcock, C.E., Shuai, Y., 2012. Evaluation of Moderate-resolution Imaging
792 Spectroradiometer (MODIS) snow albedo product (MCD43A) over tundra. *Remote Sens.*
793 *Environ.* 117, 264–280. doi:10.1016/j.rse.2011.10.002

794 Wang, Z., Schaaf, C.B., Strahler, A.H., Chopping, M.J., Rom n, M.O., Shuai, Y., Woodcock,
795 C.E., Hollinger, D.Y., Fitzjarrald, D.R., 2014. Evaluation of MODIS albedo product
796 (MCD43A) over grassland, agriculture and forest surface types during dormant and snow-
797 covered periods. *Remote Sens. Environ.* 140, 60–77. doi:10.1016/j.rse.2013.08.025

798 Woodcock, C.E., Strahler, A.H., Jupp, D.L.B., 1988a. The use of variograms in remote sensing:
799 I. Scene models and simulated images. *Remote Sens. Environ.* 25, 323–348.
800 doi:10.1016/0034-4257(88)90108-3

801 Woodcock, C.E., Strahler, A.H., Jupp, D.L.B., 1988b. The use of variograms in remote sensing:
802 II. Real digital images. *Remote Sens. Environ.* 25, 349–379. doi:10.1016/0034-
803 4257(88)90109-5

804 Zhang, X., Friedl, M. a., Schaaf, C.B., Strahler, A.H., Hodges, J.C.F., Gao, F., Reed, B.C.,
805 Huete, A., 2003. Monitoring vegetation phenology using MODIS. *Remote Sens. Environ.*
806 84, 471–475. doi:10.1016/S0034-4257(02)00135-9

807 Zhang, X., Friedl, M.A., Schaaf, C.B., 2006. Global vegetation phenology from Moderate
808 Resolution Imaging Spectroradiometer (MODIS): Evaluation of global patterns and
809 comparison with in situ measurements. *J. Geophys. Res. G Biogeosciences* 111.
810 doi:10.1029/2006JG000217

811 Zhang, X., Wang, J., Gao, F., Liu, Y., Schaaf, C., Friedl, M., Yu, Y., Jayavelu, S., Gray, J., Liu,
812 L., Yan, D., Henebry, G.M., 2017. Exploration of scaling effects on coarse resolution land
813 surface phenology. *Remote Sens. Environ.* 190, 318–330. doi:10.1016/j.rse.2017.01.001

814 Zhu, X., Chen, J., Gao, F., Chen, X., Masek, J.G., 2010. An enhanced spatial and temporal
815 adaptive reflectance fusion model for complex heterogeneous regions. *Remote Sens.*
816 *Environ.* 114, 2610–2623. doi:10.1016/j.rse.2010.05.032

817 Zurita-Milla, R., Kaiser, G., Clevers, J.G.P.W., Schneider, W., Schaepman, M.E., 2009.
818 Downscaling time series of MERIS full resolution data to monitor vegetation seasonal
819 dynamics. *Remote Sens. Environ.* 113, 1874–1885. doi:10.1016/j.rse.2009.04.011

